

The Crystal Structure of $\text{Rb}_2\text{Ti}_2\text{O}_5$

R. Federicci^{1*}, B. Baptiste², F. Finocchi³, A. F. Popa⁴, L. Brohan⁴, K. Beneut², P. Giura², G. Rousse^{5,6}, A. Descamps-Mandine¹, T. Douillard⁷, A. Shukla² and B. Leridon¹¹

¹ *LPEM-ESPCI Paris, PSL Research University, CNRS, Sorbonne Universités UPMC, 10 rue Vauquelin, F-75005 Paris, France*

² *IMPMC, Sorbonne Universités UPMC, CNRS, 4 place Jussieu, F-75005 Paris, France*

³ *INSP, Sorbonne Universités UPMC, CNRS, 4 place Jussieu, F-75005 Paris, France*

⁴ *Institut des Matériaux Jean Rouxel (IMN), Université de Nantes, CNRS, 2 rue de la Houssinière, BP 32229, F-44322 Nantes Cedex 3, France*

⁵ *UMR 8260, "Chimie du Solide et Energie", Collège de France, Sorbonne Universités UPMC, 11 Place Marcelin Berthelot, 75231 Paris Cedex 05, France*

⁶ *Réseau sur le Stockage Electrochimique de l'Energie (RS2E), FR CNRS 3459, France*

⁷ *Université de Lyon, INSA Lyon, CNRS, MATEIS, UMR 5510, F-69621 Villeurbanne, France*

(Dated: March 16, 2017)

Recent results have demonstrated an exceptionally high dielectric constant in the range 200 K-330 K in a crystalline titanium oxide : $\text{Rb}_2\text{Ti}_2\text{O}_5$. In this article, the possibility of a structural transition giving rise to ferroelectricity is carefully inspected. In particular X-Ray diffraction, high resolution transmission electron microscopy and Raman spectroscopy are performed. The crystal structure is shown to remain invariant and centrosymmetric at all temperatures between 90 K and 450 K. The stability of the $C2/m$ structure is confirmed by DFT calculations. These important findings allow to discard the existence of a conventional ferroelectric phase transition as a possible mechanism for the unusual dielectric constant observed in this material.

I. INTRODUCTION

The investigation of new layered materials has always been topical in condensed matter, since many electronic properties are marginally true in two dimensions. On the other hand, ternary titanium oxydes, such as perovskite, are known to exhibit many remarkable electronic behaviors such as ferroelectricity^{1,2}, pyroelectricity^{3,4}, colossal magnetoresistance⁵ or 2D-superconducting properties⁶. The ternary titanium oxide family denoted by $\text{M}_2\text{Ti}_n\text{O}_{2n+1}$ (MTO) with $\text{M} = \text{Li}, \text{Na}, \text{K}, \text{Rb}, \text{Cs}, \text{Fr}$ and called the Anderson-Wadsley type alkali titanates⁷ with layered structure for $2 \leq n \leq 5$ and tunnel structure for $6 \leq n \leq 8$, are known for presenting ferroelectric phase transitions, with especially high Curie temperatures² as well as for other applications⁸. Their ease of synthesis and their potential applications are a motivation to study this family of compounds.

Very few information has been reported to date in the literature concerning the $\text{Rb}_2\text{Ti}_2\text{O}_5$ (RTO) compound, which is reputed to be a layered material. Actually, two early documents report its synthesis and claim a space group Cm for its structure^{9,10}.

Earlier structural investigations were led on $\text{K}_2\text{Ti}_2\text{O}_5$, where the space group is reported to be $C2/m$ and more generally on the $\text{M}_2\text{Ti}_2\text{O}_5$ material family (MTO)^{7,11,12}. The material exhibits a five-fold coordination for titanium, which comes as a surprise since

titanium atoms tend to adopt an energetically more stable six-fold coordination in most materials¹¹. As a matter of fact, the five-fold Ti coordination has only been reported in MTO. According to the literature, this family of compounds offers a certain interest for chemists because of their oxidation abilities^{13,14} but electrical properties measurements have not been reported so far.

Recent work¹⁵ has demonstrated superionic conductivity properties attesting of an electrolyte nature of the material due to ionic electromigration. The ionic conductivity in the temperature range between 200 K and 330 K reaches as high as $10^{-3} \text{ S.cm}^{-1}$. This high ionic conductivity coupled with an electronically insulating nature leads to an electrolyte behavior. These two properties were demonstrated to yield important polarization phenomena with colossal dielectric constant reaching 10^9 at low frequency¹⁵.

However since these observations are also consistent with ferroelectric like behavior, the question of a possible associated structural phase transition arises, as an alternative explanation.

In the present work, we report a systematic characterization of the $\text{Rb}_2\text{Ti}_2\text{O}_5$ crystal structure as a function of temperature. X-ray diffraction and Raman spectroscopy techniques were both used in conjunction with theoretical calculations of structural and vibrational properties, using density functional theory.

II. CHEMICAL SYNTHESIS

The synthesis of the $\text{Rb}_2\text{Ti}_2\text{O}_5$ was made under air by melting TiO_2 (rutile) and RbNO_3 powders in a crucible.

It resulted hard aggregates of transparent needles that were kept under dry argon atmosphere in order to avoid hydration.

The crystals extracted from the aggregate exhibit a needle-shape with typically 1 millimeter length and hundreds of micrometers width and thickness.

III. CHARACTERIZATION

III.1. Single crystal XRD

Single-crystal X-ray diffraction data were acquired on an Oxford Diffraction Xcalibur-S diffractometer equipped with a Sapphire CCD-detector with Mo $K\alpha_1$ radiation ($\lambda = 0.71073 \text{ \AA}$, graphite monochromator) at 293 K. Data reduction, cell refinement, space group determination, scaling, and empirical or analytical absorption correction were performed using CrysAlisPro software¹⁶.

Aquisitions were realized at 400 K, 300 K and 150 K and they all show the same structure. The atomic positions and the lattice parameters of the $\text{Rb}_2\text{Ti}_2\text{O}_5$ structure are respectively reported in the table I and II.

III.2. Powder XRD

The X-ray powder diffraction (XRD) patterns were recorded at the IMPMC (Pierre and Marie Curie University, Paris) x-ray diffraction platform using an XPert Pro Panalytical diffractometer equipped with a Cu $K\alpha$ radiation source ($\lambda_{K\alpha 1} = 1.54056 \text{ \AA}$, $\lambda_{K\alpha 2} = 1.54439 \text{ \AA}$) with an XCelerator detector. The measurements were conducted under nitrogen atmosphere (under vacuum for 100 K acquisition) in an Anton Paar HTK 450 temperature controlled chamber. Rietveld refinements¹⁷ were performed with the FullProf suite of programs¹⁸ on X-ray powder diffraction patterns recorded in Bragg-Brentano geometry. The background was modeled using a 12-coefficients polynomial, and Thomson-Cox-Hasting Voigt functions⁷ were used as peak shape functions. Preferred orientation, consistent with a platy habit of crystallites, was taken into account in the refinements as all (001) reflections were over-estimated. Measurements in capillary would have limited this effect but they were not possible since the Bragg Brentano (reflection) geometry was imposed by our cryostat. However, these refinements reveal that the single crystal structure is representative of the whole

sample and further confirm the absence of structural transition from 100 K to 400 K. Vesta software¹⁹ was used to visualize the crystal structures. These measurements were made as function of temperature and under a nitrogen atmosphere.

The evolution of the diffractograms acquired on a RTO is pictured in figure 1 as function of temperature between 100 K and 400 K. Table III displays the lattice parameters deduced from Rietveld refinements performed on the X-ray Powder Pattern.

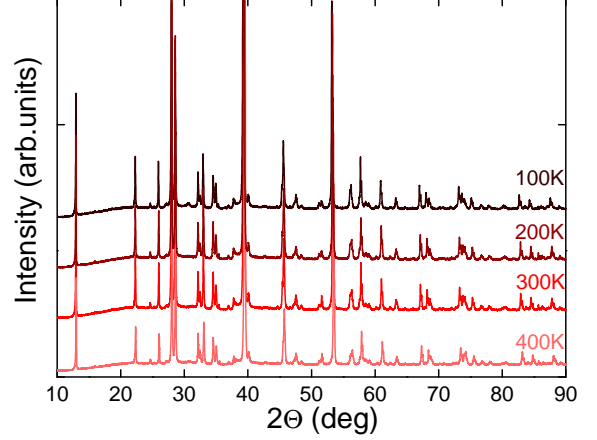


Figure 1. Diffractograms acquired on $\text{Rb}_2\text{Ti}_2\text{O}_5$ powder as function of temperature between 100 K and 400 K.

The atomic positions and lattice parameters extracted from the single crystal and the powder measurements were found to be similar and allow to conclude with a $C2/m$ structure which remains unchanged over the investigated range of temperature. The unit cell content of the RTO is shown in figure 2 using VESTA software.

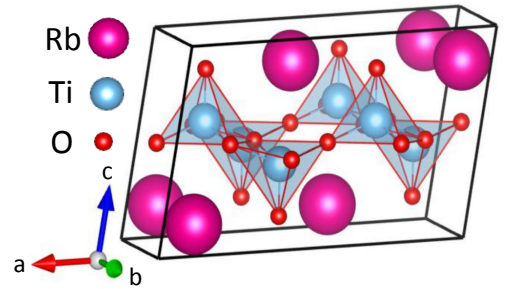


Figure 2. Structure of $\text{Rb}_2\text{Ti}_2\text{O}_5$ visualized by VESTA¹⁹ software. The Rb atoms are shown in pink, the Ti atoms in blue and the O atoms in red.

The structure of RTO is highly anisotropic. This two-dimensional structure consists in alternate layers of Ti-O and Rb atoms along the c-axis. The Ti-O

Temperature	400 K	300 K	150 K
CCDC number	1517161	1517160	1517159
Molecular Weight (g.mol ⁻¹)	346.74	346.74	346.74
Cryst syst	monoclinic	monoclinic	monoclinic
Space group	<i>C2/m</i>	<i>C2/m</i>	<i>C2/m</i>
a/Å	11.3419(12)	11.3370(13)	11.3457(12)
b/Å	3.8198(5)	3.8244(5)	3.8195(5)
c/Å	7.0103(8)	6.9946(8)	6.9699(8)
α/deg	90	90	90
β/deg	100.298(11)	100.308(12)	100.359(11)
γ/deg	90	90	90
Volume/Å ³	298.82(6)	298.37(6)	297.12(6)
Z	2	2	2
ρ _{calc} (mg.mm ⁻³)	3.854	3.860	3.876
μ (mm ⁻³)	18.796	18.824	18.903
F(000)	316.0	316.0	316.0
Crystal size	0.2 × 0.1 × 0.05	0.2 × 0.1 × 0.05	0.2 × 0.1 × 0.05
Radiation	MoKα (λ = 0.71073)	MoKα (λ = 0.71073)	MoKα (λ = 0.71073)
2θ range	5.906 to 64.994 °	5.92 to 52.726 °	5.942 to 52.714 °
Reflexions collected	1859	1389	1205
Data/restraints/param.	567/0/30	351/0/29	348/0/29
GOF on F ²	1.081	1.173	1.109
R1/wR2 (I>=2σ (I))	0.0353 /0.0893	0.0279 /0.0714	0.0499/0.1310
R1/wR2 (all)	0.0400/0.0918	0.0293/0.0725	0.0537/0.1342
Largest diff. peak/hole / eÅ ³	0.82/-1.63	0.68/-1.45	1.52/-1.93

Table I. Measurements Conditions and Crystallographic Data for Room-Temperature Single-Crystal X-ray Diffraction on Rb₂Ti₂O₅ under nitrogen at 400 K, 300 K and 150 K.

	Atom	x	y	z	U(eq)
400 K	Rb1	981.2(8)	5000	8472.5(12)	14.9(5)
	Ti1	3522.9(14)	5000	5897(2)	9.7(5)
	O1	5000	5000	5000	15(2)
	O2	3767(6)	5000	8391(9)	15.6(15)
	O3	1772(6)	5000	4776(9)	14.9(14)
300 K	Rb1	985.1(5)	5000	8481.2(8)	21.0(3)
	Ti1	3524.9(8)	5000	5884.9(14)	10.8(3)
	O1	5000	5000	5000	19.7(13)
	O2	3762(4)	5000	8367(6)	20.7(9)
	O3	1780(3)	5000	4797(5)	14.3(8)
150 K	Rb1	981.2(8)	5000	8472.5(12)	14.9(5)
	Ti1	3522.9(14)	5000	5897(2)	9.7(5)
	O1	5000	5000	5000	15(2)
	O2	3767(6)	5000	8391(9)	15.6(15)
	O3	1772(6)	5000	4776(9)	14.9(14)

Table II. Fractional Atomic Coordinates ($\times 10^4$) and Equivalent Isotropic Displacement Parameters ($\text{\AA}^2 \times 10^3$) for Rb₂Ti₂O₅. U_{eq} is defined as 1/3 of the trace of the orthogonalised U_{ij} tensor.

layers are made of chains of double pyramids sharing corners. A double-pyramid is formed by the association of two square-based pyramids sharing edges, with their apex pointing to opposite directions. In this configuration each Ti atom is surrounded by five oxygens which form a slightly tilted square based pyramid. Rb⁺ atoms sit in between those

layers. The refinements performed demonstrated that the structure is identical with the one reported for K₂Ti₂O₅¹².

III.3. Scanning electron microscopy

Rightafter the chemical synthesis process reached back room temperature, RTO crystals were isolated and Scanning Electron Microscopy (SEM) acquisitions were realized. Two SEM pictures which show the needle shape of the RTO and its lamellar structure are displayed in figure 3.

The growth direction is along the b axis. In these pictures the microscopic layered nature of the material is observable at the macroscopic scale over the entire size of the crystal. Figure 3.a displays a good overview of the superimposition of layers.

III.4. High-resolution transmission electron microscopy

Pictures of High-resolution transmission electron microscopy (HRTEM) were performed on a RTO sample (HR-TEM JEM-2010F; JEOL Ltd, Tokyo, Japan). The figure 4 pictured one of those acquisitions.

Temperature	400 K	300 K	200 K	100 K
Space group	$C2/m$	$C2/m$	$C2/m$	$C2/m$
a (Å)	11.34378(2)	11.34378(2)	11.34381(2)	11.34265(3)
b (Å)	3.82824(5)	3.82905(6)	3.82756(5)	3.82557(6)
c (Å)	6.99109(5)	7.00371(5)	6.98718(5)	6.96969(6)
β (deg)	100.2889(5)	100.2413(6)	100.2939(6)	100.3379(7)
Volume (Å ³)	298.762(7)	299.365(8)	298.495(7)	297.521(9)
R_{Bragg} (%)	9.86	13.4	12.1	13

Table III. Results of the Rietveld Refinement on the X-ray Powder Pattern of $\text{Rb}_2\text{Ti}_2\text{O}_5$ at different temperatures.

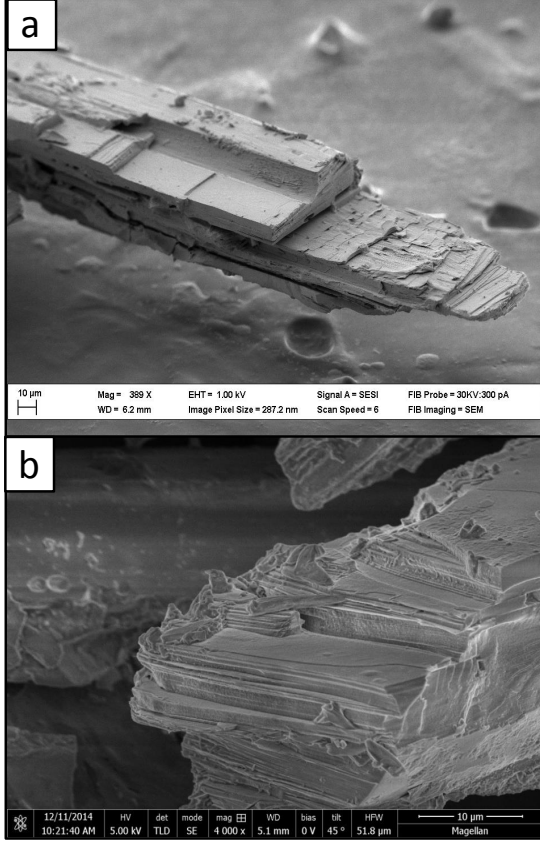


Figure 3. SEM pictures acquired on two different $\text{Rb}_2\text{Ti}_2\text{O}_5$ crystals from different batches isolated just after the chemical synthesis process reached back room temperature.

tions.

A close-up of the crystal ordering is shown in the inset of figure 4. A simulated crystal structure realized by VESTA is surimposed over the HRTEM image pointing to the crystal of the studied sample. The zig-zag light spot lines represent the (ab) plane made of the Ti-O squared base-pyramids as can attest the insert surimposed structure. Very shady lights in between these light lines show the presence of rubidium atoms forming the layers separating the Ti-O plans.

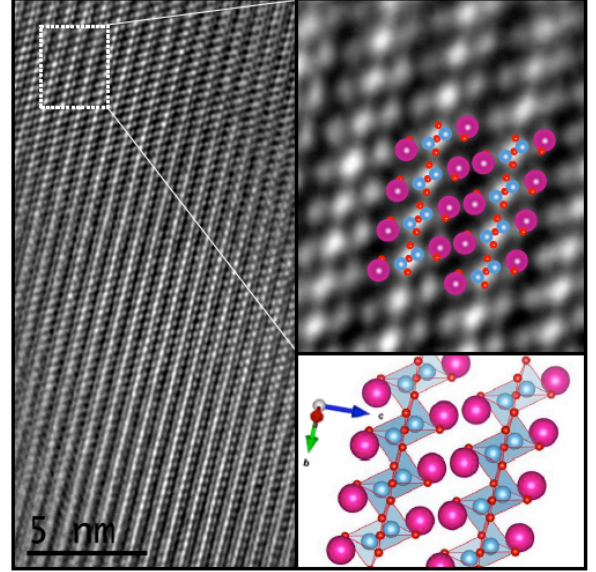


Figure 4. High resolution transmission electron microscopy image acquired on a $\text{Rb}_2\text{Ti}_2\text{O}_5$ sample along the [110] zone axis (HR-TEM JEM-2010F; JEOL Ltd, Tokyo, Japan). A close-up of the image is showed in the insert on which is superimposed a simulated crystal structure from X-Ray diffraction data. The Rb atoms are in pink, the Ti atoms are in blue and the O atoms are in red.

IV. RAMAN SPECTROSCOPY

Raman spectroscopy measurements were performed on $\text{Rb}_2\text{Ti}_2\text{O}_5$ crystals over the range of temperature [90 K - 450 K] under controlled atmosphere conditions. The set-up consisted of an argon laser source "Spectra-physics Argon 514.5 nm", a spectrometer "T64000 HORIBA Jobin Yvon", a set of optical microscopy lens used to focus the laser beam over few micrometers and a cryostat or a cryofour "linkam FTIR 600" used to control the atmosphere and the temperature with helium. The power of the laser beam was set at 140 mW and the recording times lasted 30 sec. Each Raman spectra is an average from three distinct spectra acquired in a row.

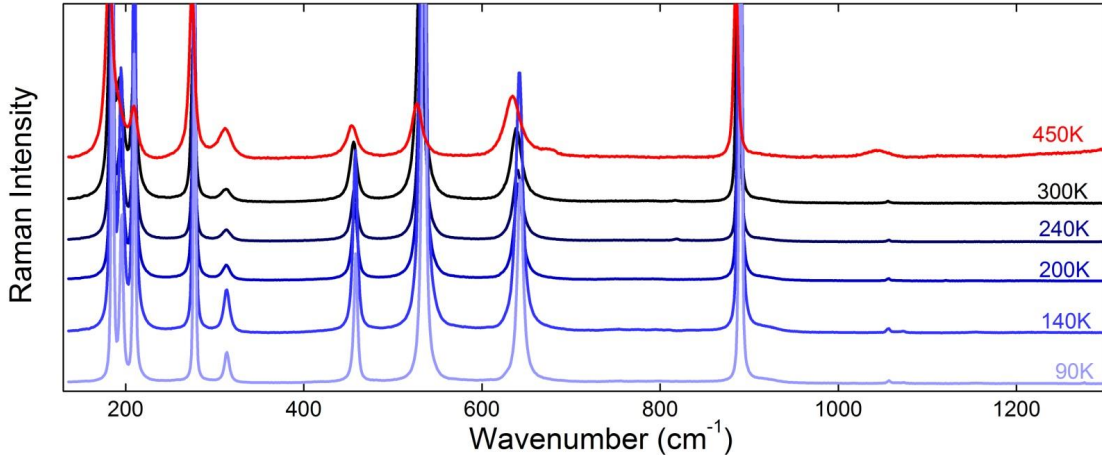


Figure 5. Experimental Raman spectra acquired on a $\text{Rb}_2\text{Ti}_2\text{O}_5$ crystal as function of the temperature under Helium atmosphere between 180 cm^{-1} and 1300 cm^{-1} . No significative changes happen when temperature decreases.

Raman spectra recorded between 90 K and 450 K over the wavenumber range $[180\text{ cm}^{-1} - 1300\text{ cm}^{-1}]$ are plotted in figure 5. The spectra remain qualitatively unchanged when temperature varies attesting of the stability of the structure over the entire explored range of temperature. Measurements were also performed at 90 K and did not show any variation of the phonon modes. This Raman spectroscopy investigation represents therefore a second probe attesting of the stability of the $C2/m$ crystal structure of the RTO material between 10 K and 450 K.

V. DENSITY FUNCTIONAL THEORY CALCULATION

V.1. Crystal structure

The structural calculations were performed on the $\text{Rb}_2\text{Ti}_2\text{O}_5$ unit cell, which consists of two formula units, through the Quantum Espresso package²⁰ that is based on the density functional theory (DFT). Both Local Density Approximation (LDA) and Generalized Gradient Approximation (GGA) functionals were used.²¹

We employed ultra-soft pseudopotentials, which include semi-core states for Rb and Ti. A Monkhorst-Pack $2 \times 6 \times 3$ grid and a cutoff energy of 50 Ryd for the expansion of the Kohn-Sham^{22,23} orbitals in plane waves (4 times as large for the charge density and potential) were enough to obtain the converged energies and the structural parameters.

At the beginning of the structural optimization, the space group was set as $C2/m$ and the atomic positions were those extracted from the X-Ray diffraction

	GGA	LDA
$a/\text{\AA}$	11.3318	11.1425
$b/\text{\AA}$	3.8322	3.7492
$c/\text{\AA}$	6.9863	6.7665
α/deg	90	90
β/deg	100.110	100.327
γ/deg	90	90
$V_0/\text{\AA}^3$	298.688	278.105
E_0/Ryd	-980.1266(6)	-980.4192(1)
B_0/GPa	53.4(0)	70.9(8)
B'_0	7.0(5)	4.5(9)

Table IV. Computed equilibrium lattice constants a , b , c and angles α , β , γ within the GGA or the LDA. The equilibrium volume V_0 , bulk modulus B_0 and its pressure derivative B'_0 have been obtained through a fit to the Murnaghan equation of state (see text).

measurements, which are displayed in Table II. Both lattice parameters, angles and atomic positions were then left free to relax; their final values, within the GGA or the LDA, are collected in Table IV. A series of structural optimizations have been conducted at several volumes around the equilibrium volume and the numerical results have been represented through the Murnaghan equation of state²⁴, via the fitted equilibrium volume V_0 , bulk modulus B_0 and its pressure derivative B'_0 .

The computed atomic positions are reported in table V. We see that the structural parameters that were computed within the GGA are extremely close to their experimental counterparts that are collected in Tab I. The computed enthalpy of formation of $\text{Rb}_2\text{Ti}_2\text{O}_5$ at zero pressure from the elementary stable phases $\text{Rb}_{(s)}$, $\text{Ti}_{(s)}$ and $\text{O}_{2(gas)}$ is -309.8 kJ/mol, within the GGA. These theoretical calculations thus

Atom	x	y	z
Rb	1003	5000	8500
Ti	3521	5000	5900
O1	5000	5000	5000
O2	3745	5000	8400
O3	1776	5000	4787

Table V. Fractional Atomic Coordinates ($\times 10^4$) after structural relaxation for the $\text{Rb}_2\text{Ti}_2\text{O}_5$ crystal, within the GGA.

confirm that the synthesized $\text{Rb}_2\text{Ti}_2\text{O}_5$ crystal is thermodynamically stable and that its structure can be solved with a high level of accuracy by combining X-ray diffraction with DFT calculations.

V.2. Band structure

The band structure pictured in the figure 6 is calculated using the GGA functional for the corresponding optimized crystal structure. The path used along the Brillouin zone is chosen using the MCL structure²⁵. A gap of at least 3.54 eV, which is likely underestimated as usual in the DFT-GGA, attests nevertheless of the insulating nature of the $\text{Rb}_2\text{Ti}_2\text{O}_5$ crystal.

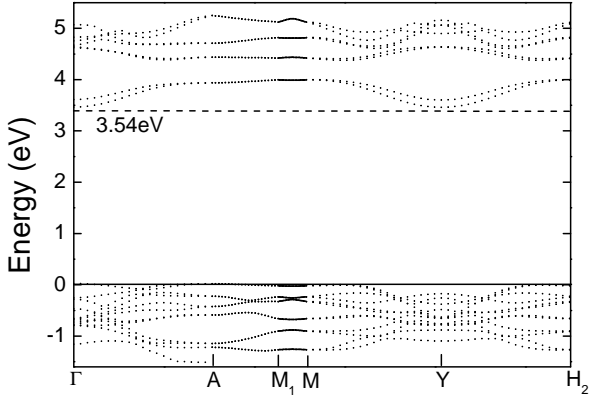


Figure 6. Band structure of $\text{Rb}_2\text{Ti}_2\text{O}_5$ calculated with GGA functional. The high-symmetry points are chosen following the path of the MCL structure²⁵. The highest occupied electronic level in the valence band is set at zero, while the dashed line makes the lowest electronic level in the conduction band.

V.3. Phonon modes

Phonon mode calculations are based on the density functional Perturbation Theory²⁶. These calculations were performed by using LDA or GGA functionals and

carried out at the corresponding relaxed structures. The phonon frequencies at the center of the Brillouin zone were computed with ultrasoft pseudopotentials, while the Raman intensities were estimated by employing norm-conserving pseudopotentials on top of the phonon calculations, and are therefore less accurate than the frequencies themselves. The theoretical phonon spectra are convolved with Lorentzians and plotted in figure 7. The Raman intensities and the phonon frequencies are extracted from the DFT calculations whereas the full width at half maximum are arbitrary chosen as 1 to make them discernable.

The red and blue curves represent the theoretical Raman spectra simulated with the GGA or the LDA functionals, respectively. The black square curve represents the experimental data recorded on a crystal of $\text{Rb}_2\text{Ti}_2\text{O}_5$ at room conditions between 180 cm^{-1} and 1300 cm^{-1} . With respect to the experimental data, the computed frequencies are higher in the LDA and lower in the GGA. This can be linked to the fact that the LDA generally underestimates the lattice parameters and provides stiffer force constants, while the GGA makes the reverse. When looking at the high-frequency part of the spectrum, the four phonon modes are bracketed by the theoretical phonon modes found with GGA and LDA functionals, which differ by not more than 56 cm^{-1} . These four phonon modes are denoted ν_1 , ν_2 , ν_3 and ν_4 , from small to high frequencies. The representations of these four phonon modes are sketched in figure 8. They all correspond to vibration modes of Ti-O bonds.

At low frequencies, ten theoretical modes were computed between 80 cm^{-1} and 330 cm^{-1} . They can be unambiguously linked to the set of experimental modes in the same wavenumber range, even though their intensities do not match with the experimental ones. The representations of all the calculated phonon modes are displayed in the supplemental material, in figures 15, 16, 17, 18, 19, 20 and 21.

Overall, the good agreement between the calculated phonon spectra for the simulated RTO system and the Raman spectra taken on a RTO crystal confirms that each mode can be assigned and analyzed in terms of a consistent set of atomic displacements and excludes the presence of singularities.

The computed diagonal effective charges for Ti are $Z_{xx}^* = 4.71$, $Z_{yy}^* = 4.72$, $Z_{zz}^* = 3.08$, with much smaller off-diagonal elements Z_{xz}^* and Z_{zx}^* . In contradiction to typical ferroelectric crystals such as BaTiO_3 ²⁷, the effective charges do not show a relevant anomalous contribution, which is consistent with the absence of an electric-driven instability in $\text{Rb}_2\text{Ti}_2\text{O}_5$.

VI. RELATION WITH ELECTRICAL PROPERTIES

As reported earlier¹⁵, the remarkable electrical properties of RTO are strongly enhanced for samples

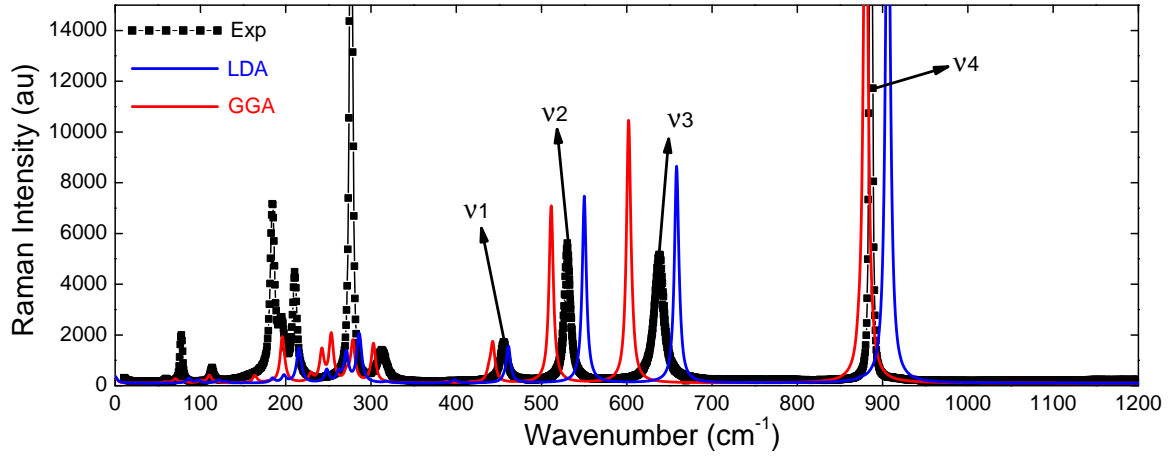


Figure 7. Experimental and simulated Raman spectra. The black square curve is the experimental Raman spectrum between 10 cm^{-1} and 1200 cm^{-1} acquired on a crystal of $\text{Rb}_2\text{Ti}_2\text{O}_5$ under room conditions. The blue curve is the theoretical raman spectrum simulated with DFT using LDA functional and the red curve using GGA functional.

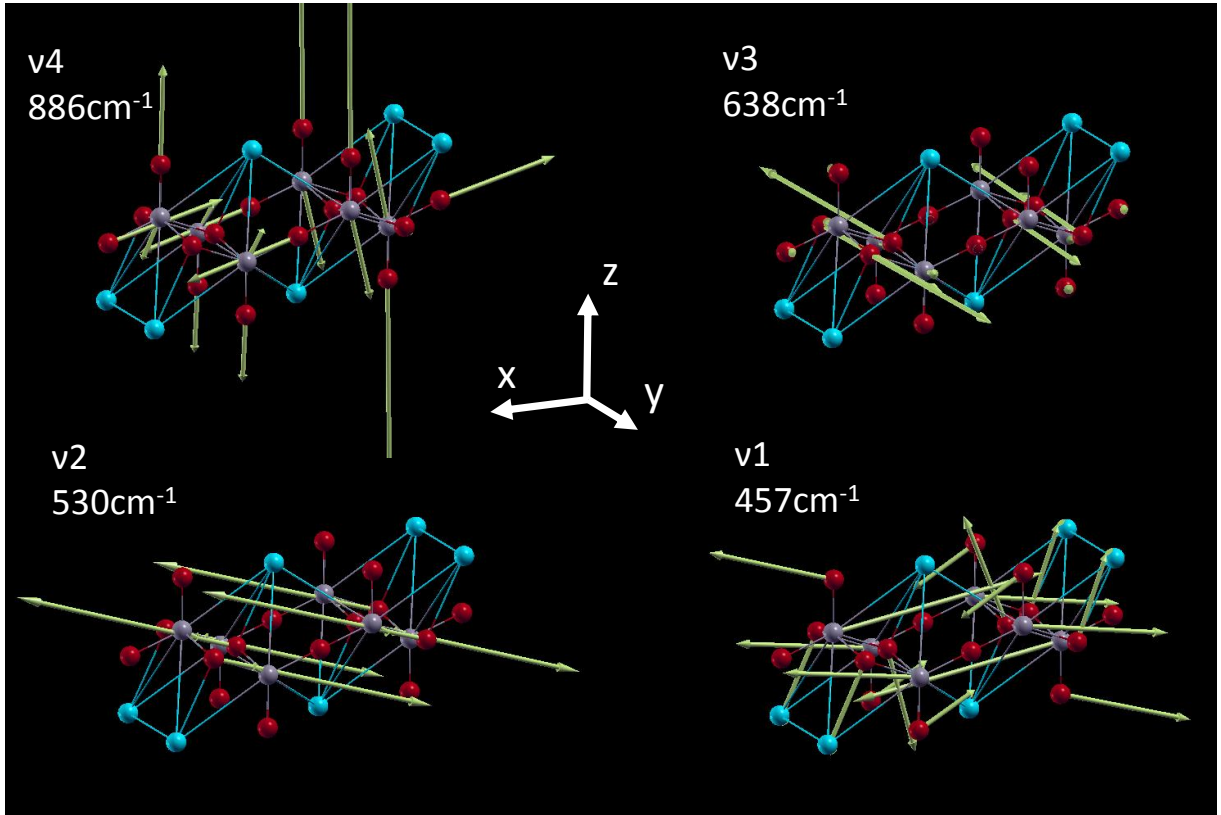


Figure 8. Representations of the vibrational phonon modes N° 54, 46, 45 and 42 calculated with density function theory for $\text{Rb}_2\text{Ti}_2\text{O}_5$ system using generalized gradient approximation. The Raman intensities are displayed in Appendix B in the table XII

annealed under vacuum at 400 K for a couple of hours. As a matter of fact, these electrical properties can also be "desactivated" when the material is annealed under 1 bar-oxygen atmosphere at 400 K. This observation tends to indicate that the existence

of such electrical properties is corroborated with the presence of oxygen vacancies in the material. In addition, the figure 9 shows that a reversible change of color operates when the material is alternatively annealed under vacuum and oxygen at 400 K. This

is a strong proof of the creation of oxygen vacancies since the material turns from white to yellow and yellow to white, similarly to what is known in TiO_2 ²⁸.

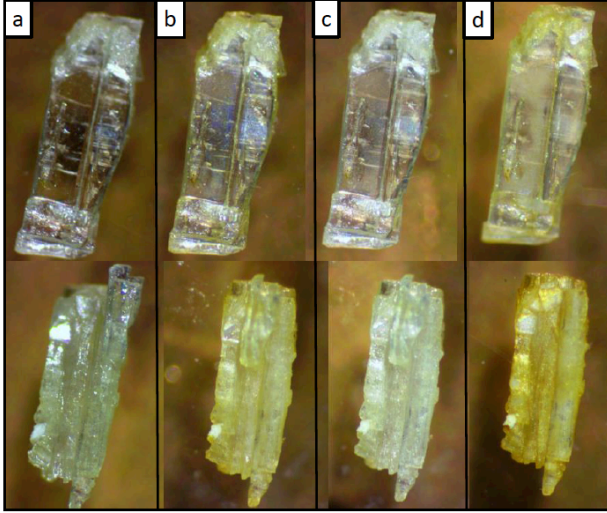


Figure 9. Change of color observed when the material is alternatively annealed for two hours under vacuum and oxygen at 400 K.

DRX investigation has thus been performed on RTO powder that was annealed *in situ* in the diffraction chamber under N_2 atmosphere. The corresponding diffractogram is displayed in figure 10 and does not show any changes as function of the temperature excepted for the apparition of a diffraction peak around 24 degree below 250 K, artifact due to a small contamination with ice into the diffraction chamber. Powder diffraction at room temperature was also performed on samples annealed for 24 hours at 400 K under vacuum and again, the same crystal structure as in as-grown crystals was found.

The powder diffraction realized on as grown samples and displayed in Tab III shows that the lattice parameters are not decreasing/increasing monotonously as expected as function of the temperature because of the thermal dilatations. The a lattice parameters decreases from 400 K to 300 K and then increases untill 100 K, while b does the contrary and c decreases regularly. This behavior may be due to an unusual lattice distortion which takes place roughly in the temperature range where transport and dielectric properties of the RTO are the most singular. This would deserve further investigations. Finally, it is known that X-ray diffraction can not discern the presence of oxygen vacancies into a crystal structure. Neutron diffraction will be considered in order to further investigate the presence of oxygen vacancies induced by the annealing processes.

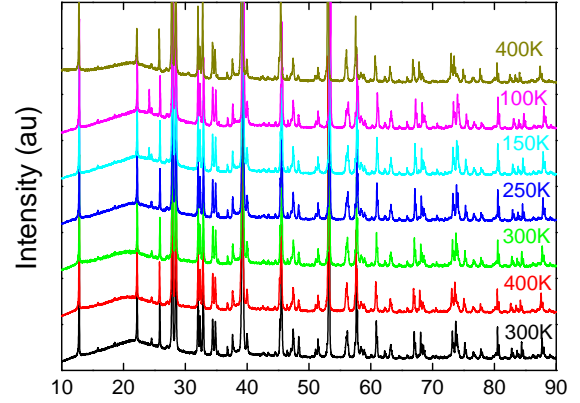


Figure 10. Powder X-ray diffractograms of $\text{Rb}_2\text{Ti}_2\text{O}_5$ and $\text{Rb}_2\text{Ti}_2\text{O}_{5-\delta}$ taken at different temperatures and displaced for clarity. From bottom to top: as-grown sample at 300 K, vacuum-annealed sample at 400 K, vacuum-annealed sample at 300 K, vacuum-annealed sample at 250 K, vacuum-annealed sample at 150 K, vacuum-annealed sample at 100 K, N_2 -annealed sample at 400 K. All annealing procedures were made *in situ*. The annealing duration was 8 hours. The pic at 24.17 deg (3.68 angstroms) comes from the formation of a very thin layer of H_2O ice on the surface of the sample. Heating the sample from 150K up to 250K under vacuum allowed us to reversibly remove the ice. This proves that the sample is not altered by the presence of this residual solid state H_2O .

VII. CONCLUSION

The crystal structure of $\text{Rb}_2\text{Ti}_2\text{O}_5$ has been characterized as a function of temperature using X-Ray diffraction and Raman spectroscopy. Both methods found the space group of the material consistent with $C/2m$ between 90 K and 450 K. The outcomes of the X-Ray diffraction and Raman spectroscopy are compared to theoretical calculations made with density functional theory and are in excellent agreement. The structure found is also confirmed by transmission electron microscopy and scanning electron microscopy.

In addition, this work shows that the $C/2m$ structure of the material remains unchanged between 90 K and 450 K, thus excluding the existence of a structural transition between 200 K and 330 K. This is true for as-grown samples as well as in "deoxygenated" vacuum-annealed or N_2 -annealed samples. These findings lead to discard a conventional ferroelectric transition as a mechanism responsible for the reported colossal polarisability of $\text{Rb}_2\text{Ti}_2\text{O}_5$.

BIBLIOGRAPHY

- ¹D. Maurya, J. Kumar, and Shripal, Journal of Applied Physics **100**, 034103 (2006), doi:

- \bibinfo doi <http://dx.doi.org/10.1063/1.2227255>, <http://scitation.aip.org/content/aip/journal/jap/100/3/10.1063/1.2227255>
- ²S. V. Vikram, D. M. Phase, and V. S. Chandel, *Journal of Materials Science: Materials in Electronics* **21**, 902 (2010), ISSN 1573-482X, <http://dx.doi.org/10.1007/s10854-009-0015-0>
- ³Y. Shaldin, S. Matyjasik, M. Tseitlin, and M. Roth, *Optical Materials* **30**, 101 (2007), ISSN 0925-3467, <http://www.sciencedirect.com/science/article/pii/S0925346706003703>
- ⁴Y. V. Shaldin, S. Matyjasik, M. Tseitlin, E. Mojaev, and M. Roth, *physica status solidi (b)* **246**, 452 (2009), ISSN 1521-3951, <http://dx.doi.org/10.1002/pssb.200844294>
- ⁵M. McCormack, S. Jin, T. H. Tiefel, R. M. Fleming, J. M. Phillips, and R. Ramesh, *Applied Physics Letters* **64**, 3045 (1994), <http://scitation.aip.org/content/aip/journal/apl/64/22/10.1063/1.111372>
- ⁶N. Reyren, S. Thiel, A. D. Caviglia, L. F. Kourkoutis, G. Hammerl, C. Richter, C. W. Schneider, T. Kopp, A.-S. Rüetschi, D. Jaccard, M. Gabay, D. A. Muller, J.-M. Triscone, and J. Mannhart, *Science* **317**, 1196 (2007), <http://science.sciencemag.org/content/317/5842/1196.full.pdf+html>
- ⁷M. Tournoux, R. Marchand, and L. Brohan, *Progress in Solid State Chemistry* **17**, 33 (1986), ISSN 0079-6786, <http://www.sciencedirect.com/science/article/pii/0079678686900038>
- ⁸Shripal, S. Badhwar, D. Maurya, and J. Kumar, *Journal of Materials Science: Materials in Electronics* **16**, 495 (2005), ISSN 1573-482X, <http://dx.doi.org/10.1007/s10854-005-2723-4>
- ⁹O. Schmitz-Dumont and A. H. Schulz, *Monatshefte für Chemie und verwandte Teile anderer Wissenschaften* **83**, 638 (1952), ISSN 1434-4475, <http://dx.doi.org/10.1007/BF00897713>
- ¹⁰O. Schmitz-DuMont and H. Reckhard, *Monatshefte für Chemie und verwandte Teile anderer Wissenschaften* **90**, 134 (1959), ISSN 1434-4475, <http://dx.doi.org/10.1007/BF00925227>
- ¹¹S. Andersson and A. D. Wadsley, *Nature* **4736** (aug 1960), doi:\bibinfo doi 10.1038/187499a0, <http://www.nature.com/nature/journal/v187/n4736/pdf/187499a0.pdf>
- ¹²S. Andersson and A. D. Wadsley, *Acta Chem. Scand* **3** (aug 1961), doi:\bibinfo doi 10.3891/acta.chem.scand.15-0663, http://acta.chemscand.org/pdf/acta_vol_15_p0663-0669.pdf
- ¹³Z. G. Qiang Wang and J. S. Chung, *Chem. Commun* **35**, 5284 (2009), <http://pubs.rsc.org/en/content/articlepdf/2009/cc/b909455e>
- ¹⁴J. S. C. Qiang Wang and Z. Guo, *Ind. Eng. Chem. Res* **50** (13), 8384 (2011), <http://pubs.acs.org/doi/abs/10.1021/ie200698j>
- ¹⁵R. Federicci, S. Holé, B. Baptiste, S. Merccone, and B. léridon(2017), <http://>
- ¹⁶Rigaku Oxford Diffraction(2015)
- ¹⁷H. M. Rietveld, *J. Appl. Crystallogr* **65–71** (1969)
- ¹⁸Rodriguez-Carvajal, *J. Phys. B* **55–69** (1993)
- ¹⁹K. Momma and F. Izumi, *Journal of Applied Crystallography* **44**, 1272 (Dec 2011), <https://doi.org/10.1107/S0021889811038970>
- ²⁰e. a. Paolo Giannozzi, *Journal of Physics: Condensed Matter* **21**, 395502 (2009), <http://stacks.iop.org/0953-8984/21/i=39/a=395502>
- ²¹J. P. Perdew, K. Burke, and M. Ernzerhof, *Phys. Rev. Lett.* **77**, 3865 (Oct 1996), <http://link.aps.org/doi/10.1103/PhysRevLett.77.3865>
- ²²P. Hohenberg and W. Kohn, *Phys. Rev.* **136**, B864 (Nov 1964), <http://link.aps.org/doi/10.1103/PhysRev.136.B864>
- ²³W. Kohn and L. J. Sham, *Phys. Rev.* **140**, A1133 (Nov 1965), <http://link.aps.org/doi/10.1103/PhysRev.140.A1133>
- ²⁴F. D. Murnaghan, *PNAS* **30**, 244 (1944), <http://www.pnas.org/content/30/9/244.citation>
- ²⁵W. Setyawan and S. Curtarolo, *Computational Materials Science* **49**, 299 (2010), ISSN 0927-0256, <http://www.sciencedirect.com/science/article/pii/S0927025610002697>
- ²⁶S. Baroni, S. de Gironcoli, A. Dal Corso, and P. Giannozzi, *Rev. Mod. Phys.* **73**, 515 (Jul 2001), <http://link.aps.org/doi/10.1103/RevModPhys.73.515>
- ²⁷P. Rabe, Karin M.and Ghosez, “First-principles studies of ferroelectricoxides,” in *Physics of Ferroelectrics: A Modern Perspective* (Springer Berlin Heidelberg, Berlin, Heidelberg, 2007) pp. 117–174, ISBN 978-3-540-34591-6, http://dx.doi.org/10.1007/978-3-540-34591-6_4
- ²⁸T. Sekiya, K. Ichimura, M. Igarashi and S. Kurita, *Journal of Physics and Chemistry of Solids* **61**, 1237–1242 (Aug 2000), <http://www.sciencedirect.com/science/article/pii/S0022369799004242>

VIII. APPENDIX A : TABLES FOR DIFFERENT XRD RESULTS

Atom	U_{11}	U_{22}	U_{33}	U_{23}	U_{13}	U_{12}
Rb1	18.9(4)	21.0(4)	24.1(4)	0	6.2(2)	0
Ti1	4.4(5)	10.2(6)	17.3(5)	0	0.7(4)	0
O1	9(3)	13(3)	40(3)	0	9(2)	0
O2	19(2)	22(3)	18.6(19)	0	-1.1(16)	0
O3	5.7(16)	12(2)	24.0(19)	0	-1.7(14)	0

Table VI. Anisotropic Displacement Parameters ($\text{\AA}^2 \times 10^3$) for $\text{Rb}_2\text{Ti}_2\text{O}_5$ at 300K. The anisotropic displacement factor exponent takes the form: $-2\pi^2(h^2a^{*2}U_{11} + 2hka^*b^*U_{12} + \dots)$.

Atom	Atom	Length(\AA)	Atom	Atom	Length(\AA)
Rb1	Rb1 ¹	3.3468(11)	Ti1	O3 ⁹	1.9861(10)
Rb1	Ti1 ²	3.5945(10)	Ti1	O3	1.988(4)
Rb1	Ti1 ³	3.5945(10)	Ti1	O3 ¹⁰	1.9861(10)
Rb1	O3	2.878(4)	Ti1	O1	1.8842(9)
Rb1	O3 ⁴	3.537(4)	Ti1	O2	1.709(4)
Rb1	O1 ²	3.1400(5)	O3	Rb1 ⁴	3.537(4)
Rb1	O1 ³	3.1400(5)	O3	Ti1 ¹⁰	1.9861(10)
Rb1	O2 ²	3.153(3)	O3	Ti1 ⁹	1.9861(10)
Rb1	O2 ⁵	2.894(3)	O1	Rb1 ⁹	3.1400(5)
Rb1	O2 ³	3.153(3)	O1	Rb1 ⁸	3.1400(5)
Rb1	O2	3.164(4)	O1	Rb1 ¹⁰	3.1400(5)
Rb1	O2 ⁶	2.894(3)	O1	Rb1 ⁷	3.1400(5)
Ti1	Rb1 ⁷	3.5945(10)	O1	Ti1 ¹¹	1.8841(9)
Ti1	Rb1 ⁸	3.5945(10)	O2	RbA ⁶	2.894(3)
Ti1	Rb1 ⁹	3.7281(10)	O2	Rb1 ⁷	3.153(3)
Ti1	Rb1 ¹⁰	3.7281(10)	O2	Rb1 ⁸	3.153(3)
Ti1	Ti1 ¹⁰	3.0920(14)	O2	Rb1 ⁵	2.894(3)
Ti1	Ti1 ⁹	3.0920(14)			

Table VII. Bond Lengths for $\text{Rb}_2\text{Ti}_2\text{O}_5$ at 300K.

¹-X,1-Y,2-Z; ²-1/2+X,-1/2+Y,+Z; ³-1/2+X,1/2+Y,+Z; ⁴-X,1-Y,1-Z; ⁵1/2-X,3/2-Y,2-Z; ⁶1/2-X,1/2-Y,2-Z;
⁷1/2+X,1/2+Y,+Z; ⁸1/2+X,-1/2+Y,+Z; ⁹1/2-X,1/2-Y,1-Z; ¹⁰1/2-X,3/2-Y,1-Z; ¹¹1-X,1-Y,1-Z

Atom	U_{11}	U_{22}	U_{33}	U_{23}	U_{13}	U_{12}
Rb1	25.2(3)	27.7(3)	28.7(3)	0	8.87(19)	0
Ti1	5.8(3)	12.6(4)	19.2(4)	0	1.6(2)	0
O1	10(2)	19(3)	48(3)	0	15(2)	0
O2	29.5(19)	24(2)	21.9(16)	0	-0.5(14)	0
O3	5.5(12)	13.6(15)	31.8(17)	0	0.2(11)	0

Table VIII. Anisotropic Displacement Parameters ($\text{\AA}^2 \times 10^3$) for $\text{Rb}_2\text{Ti}_2\text{O}_5$ at 400K. The anisotropic displacement factor exponent takes the form: $-2\pi^2(h^2a^{*2}U_{11} + 2hka^*b^*U_{12} + \dots)$.

IX. APPENDIX B : REPRESENTATIONS OF THE DFT PHONON MODES CALCULATED WITH GGA FUNCTIONAL

Atom	Atom	Length(Å)	Atom	Atom	Length(Å)
Rb1	Rb1 ¹	3.3518(10)	Ti1	O3 ⁹	1.9824(9)
Rb1	Ti1 ²	3.6000(9)	Ti1	O3	1.992(3)
Rb1	Ti1 ³	3.6000(9)	Ti1	O3 ¹⁰	1.9824(9)
Rb1	O3	2.893(4)	Ti1	O1	1.8844(8)
Rb1	O3 ⁴	3.542(3)	Ti1	O2	1.705(4)
Rb1	O1 ³	3.1464(5)	O3	Rb1 ⁴	3.542(3)
Rb1	O1 ²	3.1464(5)	O3	Ti1 ¹⁰	1.9824(9)
Rb1	O2 ²	3.154(3)	O3	Ti1 ⁹	1.9824(9)
Rb1	O2	3.164(4)	O1	Rb1 ⁷	3.1464(5)
Rb1	O2 ⁵	2.899(3)	O1	Rb1 ¹⁰	3.1464(5)
Rb1	O2 ³	3.154(3)	O1	Rb1 ⁸	3.1464(5)
Rb1	O2 ⁶	2.899(3)	O1	Rb1 ⁹	3.1464(5)
Ti1	Rb1 ⁷	3.6000(9)	O1	Ti1 ¹¹	1.8844(7)
Ti1	Rb1 ⁸	3.6000(9)	O2	Rb1 ⁶	2.899(3)
Ti1	Rb1 ⁹	3.7338(9)	O2	Rb1 ⁸	3.154(3)
Ti1	Rb1 ¹⁰	3.7338(9)	O2	Rb1 ⁵	2.899(3)
Ti1	Rb1 ¹⁰	3.0926(12)	O2	Rb1 ⁷	3.154(3)
Ti1	Rb1 ⁹	3.0926(12)			

Table IX. **Bond Lengths for for Rb₂Ti₂O₅ at 400K.**

¹-X,1-Y,2-Z; ²-1/2+X,-1/2+Y,+Z; ³-1/2+X,1/2+Y,+Z; ⁴-X,1-Y,1-Z; ⁵1/2-X,3/2-Y,2-Z; ⁶1/2-X,1/2-Y,2-Z;
⁷1/2+X,1/2+Y,+Z; ⁸1/2+X,-1/2+Y,+Z; ⁹1/2-X,1/2-Y,1-Z; ¹⁰1/2-X,3/2-Y,1-Z; ¹¹1-X,1-Y,1-Z

Atom	U ₁₁	U ₂₂	U ₃₃	U ₂₃	U ₁₃	U ₁₂
Rb1	12.3(6)	17.9(7)	13.1(6)	0	-1.6(4)	0
Ti1	5.5(9)	10.9(10)	10.5(9)	0	-4.3(6)	0
O1	6(3)	16(4)	19(3)	0	-6(3)	0
O2	13(3)	15(3)	16(3)	0	-4(3)	0
O3	4(4)	19(5)	22(5)	0	0(4)	0

Table X. **Anisotropic Displacement Parameters (Å²×10³) for Rb₂Ti₂O₅ at 150K. The anisotropic displacement factor exponent takes the form: $-2\pi^2(h^2a^{*2}U_{11} + 2hka^*b^*U_{12} + \dots)$.**

Atom	Atom	Length(Å)	Atom	Atom	Length(Å)
Rb1	Rb1 ¹	3.3460(16)	Ti1	O3	1.8910(15)
Rb1	Ti1 ²	3.5845(17)	Ti1	O3 ⁸	1.9805(17)
Rb1	Ti1 ³	3.5845(17)	Ti1	O3	2.000(6)
Rb1	O1 ²	3.1265(7)	Ti1	O3 ⁹	1.9805(17)
Rb1	O1 ³	3.1265(7)	Ti1	O2	1.710(7)
Rb1	O3 ⁴	3.513(6)	O1	Rb1 ⁷	3.1266(7)
Rb1	O3	2.877(7)	O1	Rb1 ⁹	3.1266(7)
Rb1	O2 ²	3.154(3)	O3	Ti1 ⁹	1.9824(9)
Rb1	O2	3.171(6)	O1	Rb1 ⁸	3.1266(7)
Rb1	O2 ²	3.148(5)	O1	Rb1 ¹⁰	3.1266(7)
Rb1	O2 ⁵	2.878(5)	O1	Ti1 ¹¹	1.8910(15)
Rb1	O2 ⁶	2.878(5)	O3	Rb1 ⁴	3.513(6)
Rb1	O2 ³	3.148(5)	O3	Ti ⁹	1.9805(17)
Ti1	Rb1 ⁷	3.5845(17)	O3	Ti1 ⁸	1.9805(17)
Ti1	Rb1 ⁸	3.7221(16)	O2	Rb1 ⁵	2.878(5)
Ti1	Rb1 ⁹	3.7221(16)	O2	Rb1 ⁷	3.148(5)
Ti1	Rb1 ¹⁰	3.5845(17)	O2	Rb1 ¹⁰	3.148(5)
Ti1	Ti1 ⁹	3.091(2)	O2	Rb1 ⁶	2.878(5)
Ti1	Ti1 ⁸	3.091(2)			

Table XI. **Bond Lengths for for Rb₂Ti₂O₅ at 150K.**

¹-X,1-Y,2-Z; ²-1/2+X,-1/2+Y,+Z; ³-1/2+X,1/2+Y,+Z; ⁴-X,1-Y,1-Z; ⁵1/2-X,3/2-Y,2-Z; ⁶1/2-X,1/2-Y,2-Z;
⁷1/2+X,1/2+Y,+Z; ⁸1/2+X,-1/2+Y,+Z; ⁹1/2-X,1/2-Y,1-Z; ¹⁰1/2-X,3/2-Y,1-Z; ¹¹1-X,1-Y,1-Z

N°	ν (cm ⁻¹)	Raman Intensity (au)	N°	ν (cm ⁻¹)	Raman Intensity (au)
1	0	low	28	240	high
2	0	low	29	252	medium
3	0	low	30	254	high
4	0	low	31	256	low
5	0	low	32	282	medium
6	0	low	33	292	low
7	9	low	34	301	high
8	63	low	35	309	low
9	67	low	36	319	high
10	73	low	37	387	low
11	86	low	38	400	low
12	87	low	39	413	low
13	88	low	40	432	low
14	89	low	41	444	medium
15	92	low	42	447	high
16	115	low	43	457	low
17	125	low	44	498	low
18	134	medium	45	507	high
19	145	low	46	594	high
20	155	low	47	599	medium
21	165	medium	48	624	low
22	183	low	49	721	low
23	193	low	50	759	low
24	219	high	51	759	low
25	225	medium	52	846	low
26	230	medium	53	879	medium
27	234	medium	54	881	high

Table XII. List of vibrational phonon modes calculated with the Density Functional Theory using Generalized Gradient Approximation for the Rb₂Ti₂O₅ system. High Raman intensity range : [1500 - 15000], medium Raman intensity range : [150 - 1500], low Raman intensity range : [0 - 150]. The phonon mode representations are displayed in figure 15, 16, 17, 18, 19, 20, 21

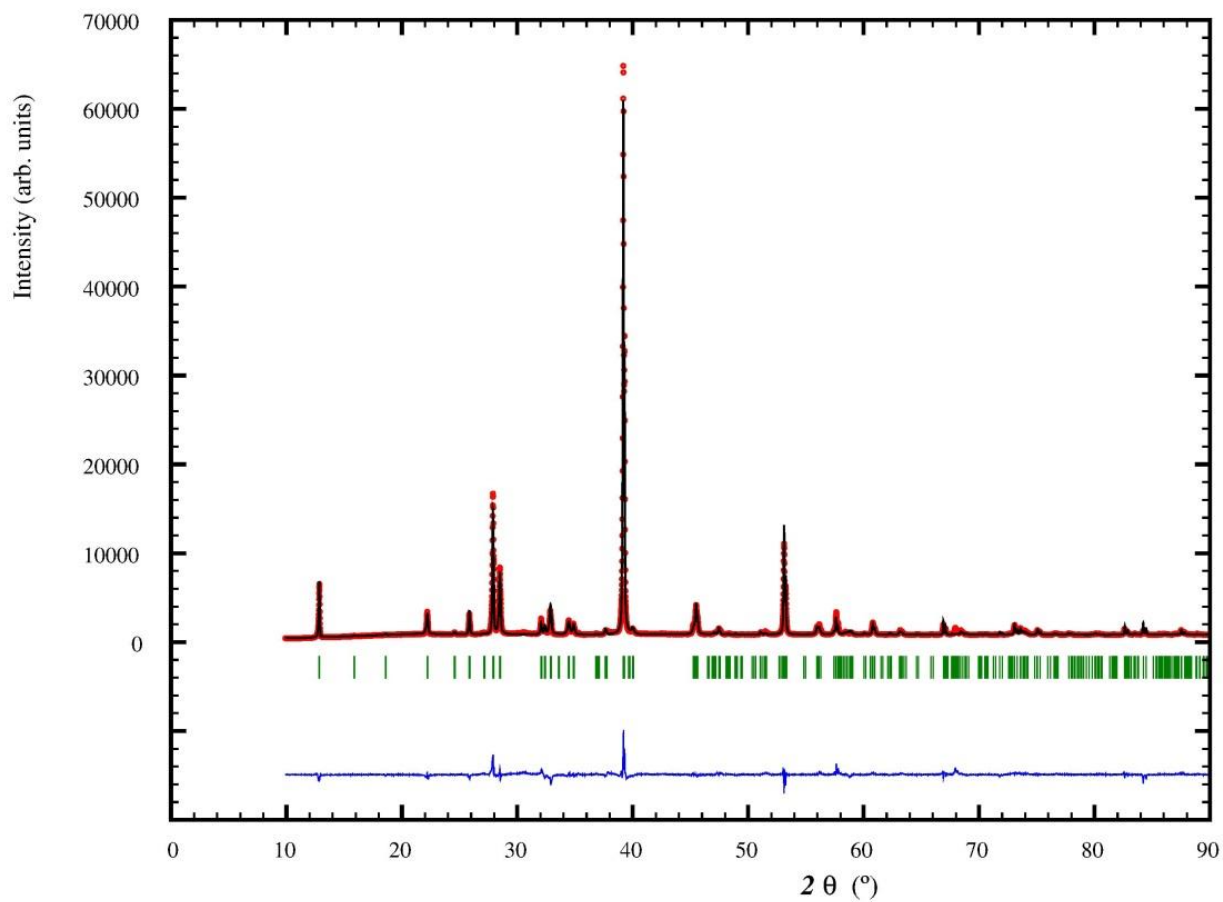


Figure 11. Rietveld refinements of the Rb₂Ti₂O₅ X-Ray powder diffraction pattern (λ_{Cu}) at 400 K. For all, the red circles are the experimental points, the black line are the calculated pattern, blue vertical tick marks refer to Bragg reflections and the blue line are the difference (observed-calculated) pattern.

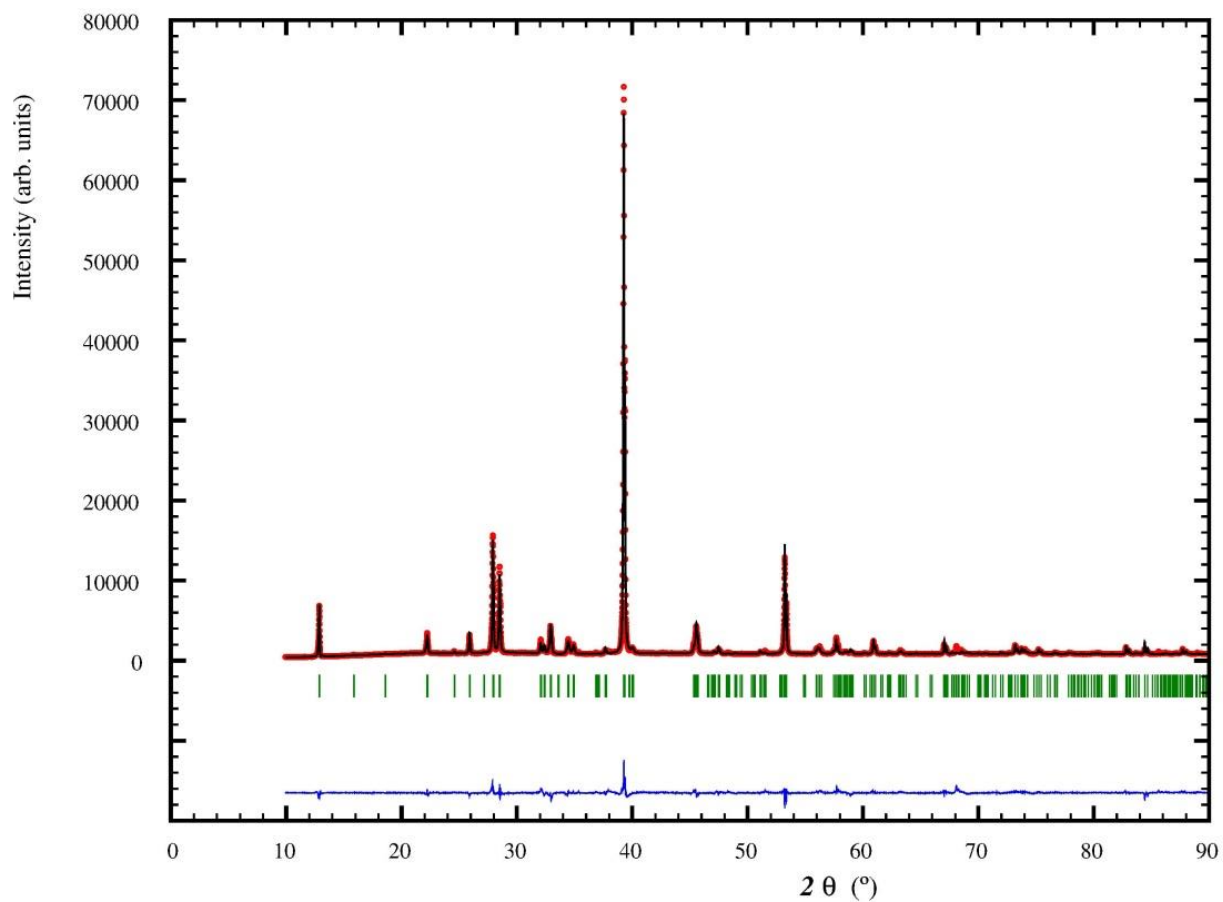


Figure 12. Rietveld refinements of the Rb₂Ti₂O₅ X-Ray powder diffraction pattern (λ_{Cu}) at 300 K. For all, the red circles are the experimental points, the black line are the calculated pattern, blue vertical tick marks refer to Bragg reflections and the blue line are the difference (observed-calculated) pattern.

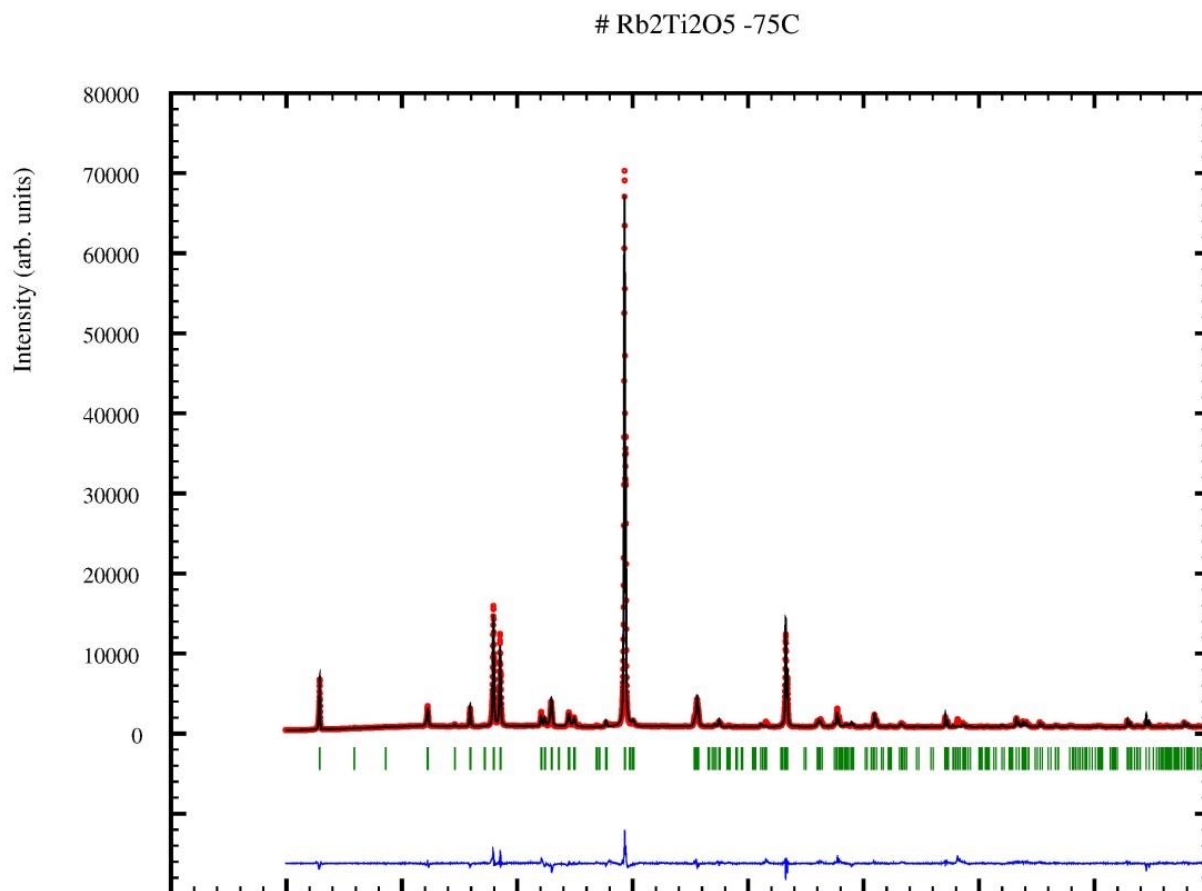


Figure 13. Rietveld refinements of the Rb₂Ti₂O₅ X-Ray powder diffraction pattern (λ_{Cu}) at 200 K. For all, the red circles are the experimental points, the black line are the calculated pattern, blue vertical tick marks refer to Bragg reflections and the blue line are the difference (observed-calculated) pattern.

Rb₂Ti₂O₅ -175C

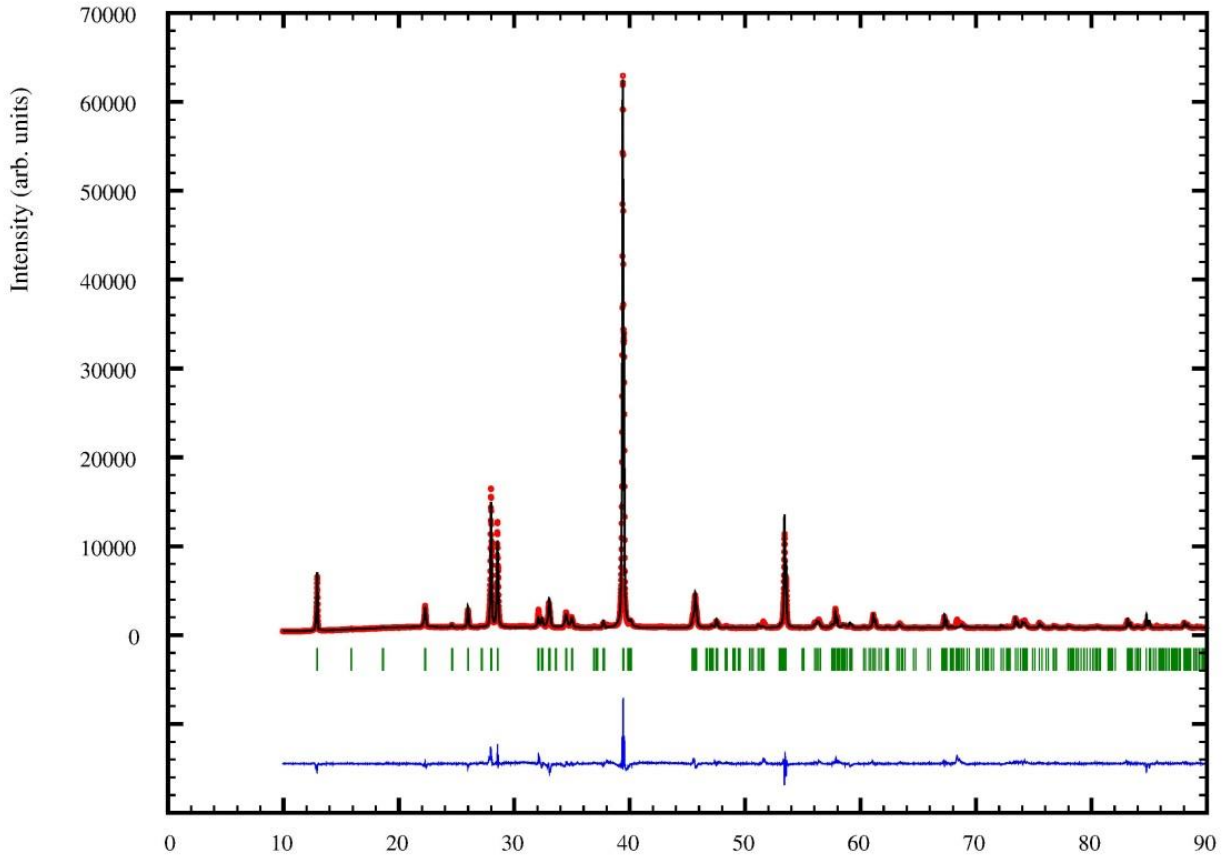


Figure 14. Rietveld refinements of the Rb₂Ti₂O₅ X-Ray powder diffraction pattern (λ_{Cu}) at 100 K. For all, the red circles are the experimental points, the black line are the calculated pattern, blue vertical tick marks refer to Bragg reflections and the blue line are the difference (observed-calculated) pattern.

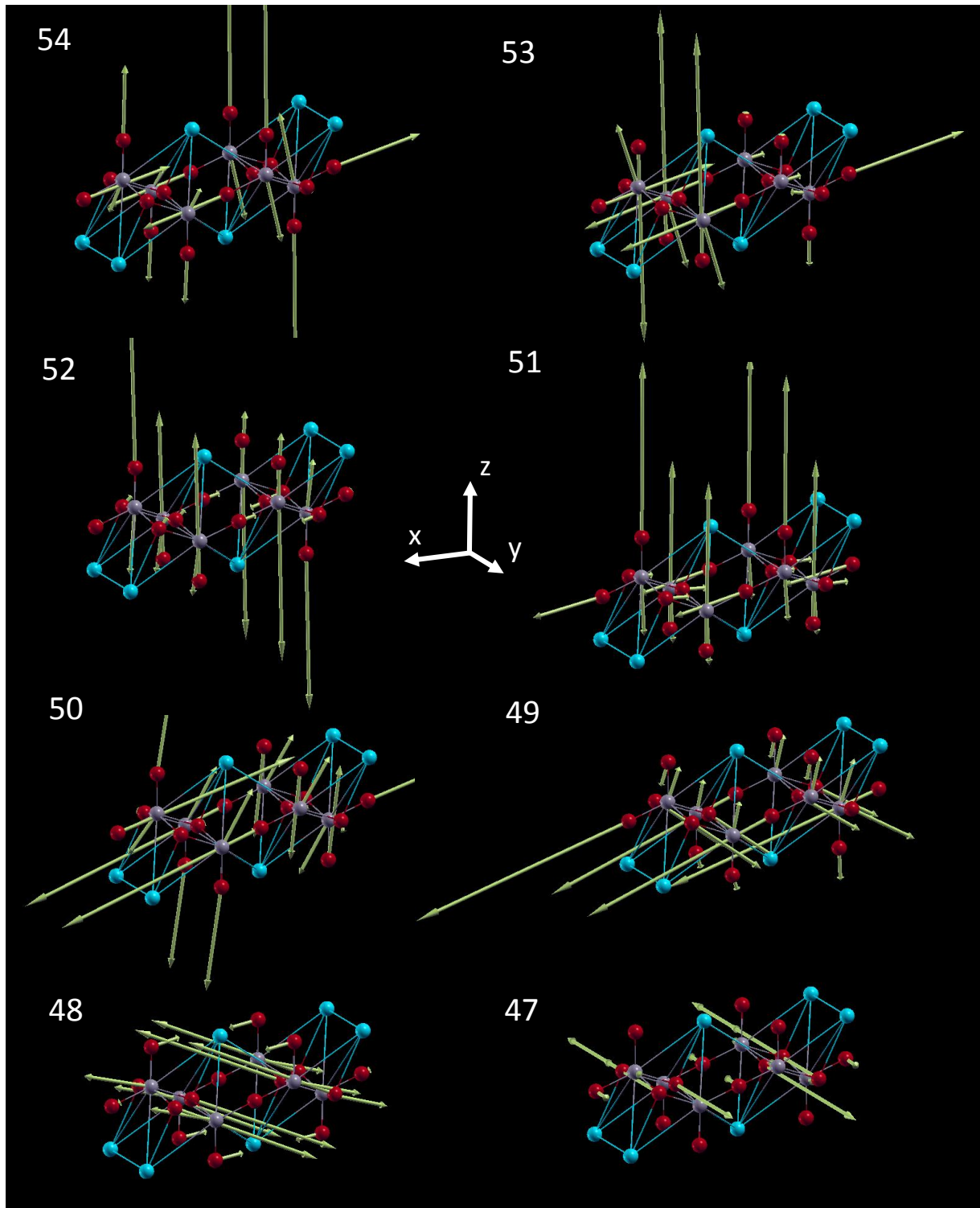


Figure 15. Representations of the vibrational phonon modes N° 54, 53, 52, 51, 50, 49, 48 and 47 calculated using Density Function Theory for $\text{Rb}_2\text{Ti}_2\text{O}_5$ system. The frequency and Raman intensity of the related phonon modes are displayed in the table [XII](#)

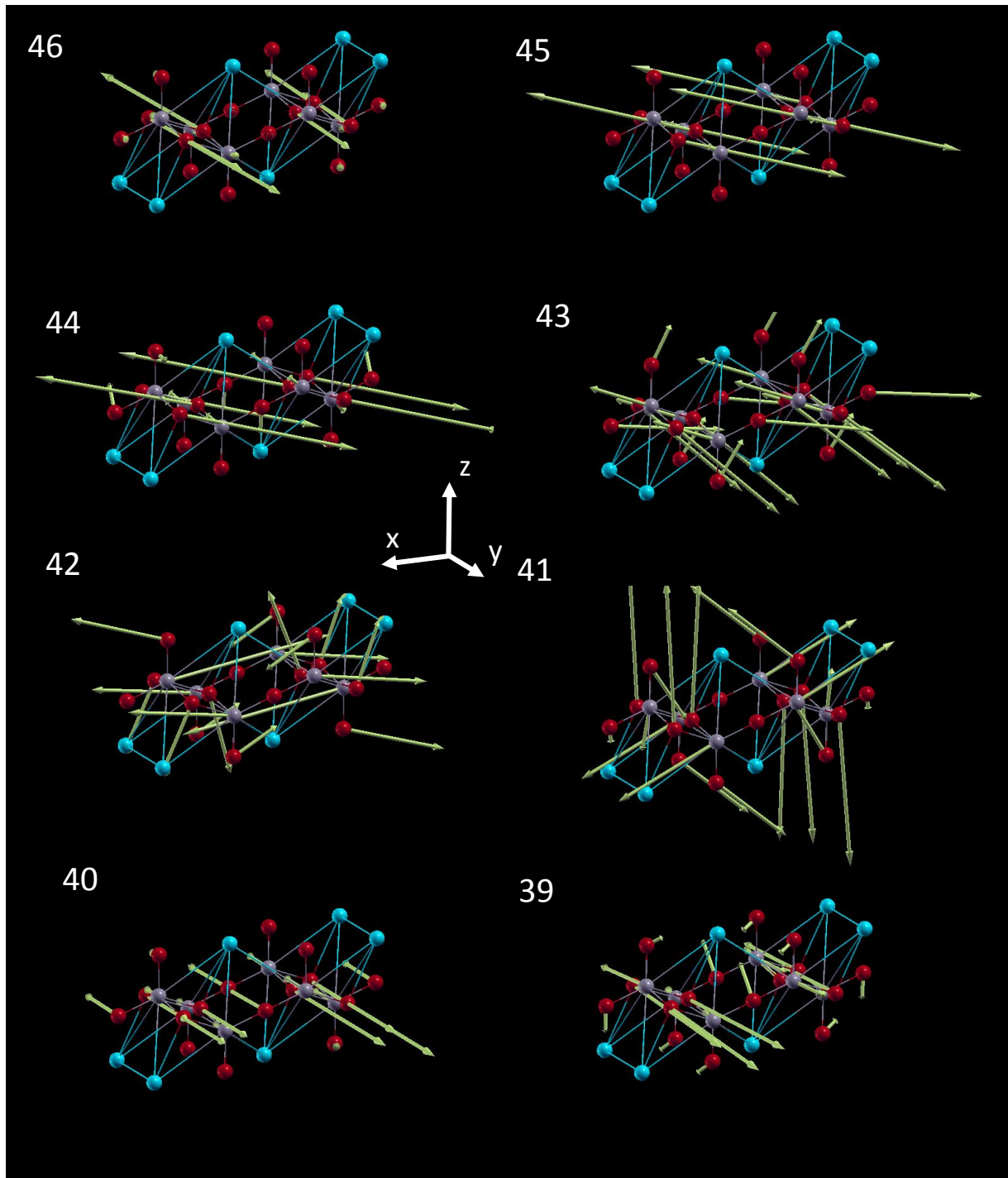


Figure 16. Representations of the vibrational phonon modes N° 46, 45, 44, 43, 42, 41, 40 and 39 calculated using Density Function Theory for $\text{Rb}_2\text{Ti}_2\text{O}_5$ system. The frequency and Raman intensity of the related phonon modes are displayed in the table [XII](#)

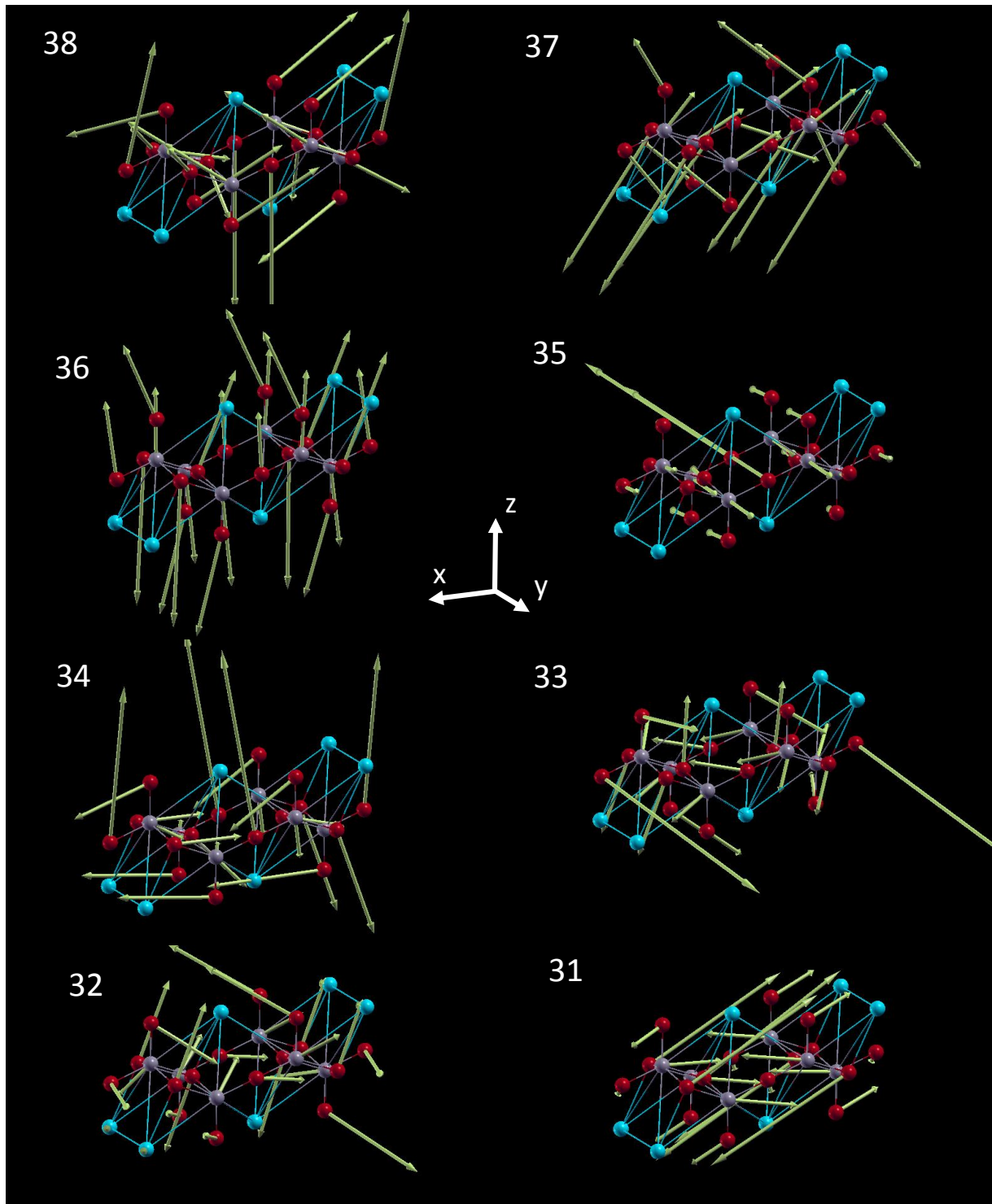


Figure 17. Representations of the vibrational phonon modes N° 38, 37, 36, 35, 34, 33, 32 and 31 calculated using Density Function Theory for $\text{Rb}_2\text{Ti}_2\text{O}_5$ system. The frequency and Raman intensity of the related phonon modes are displayed in the table [XII](#)

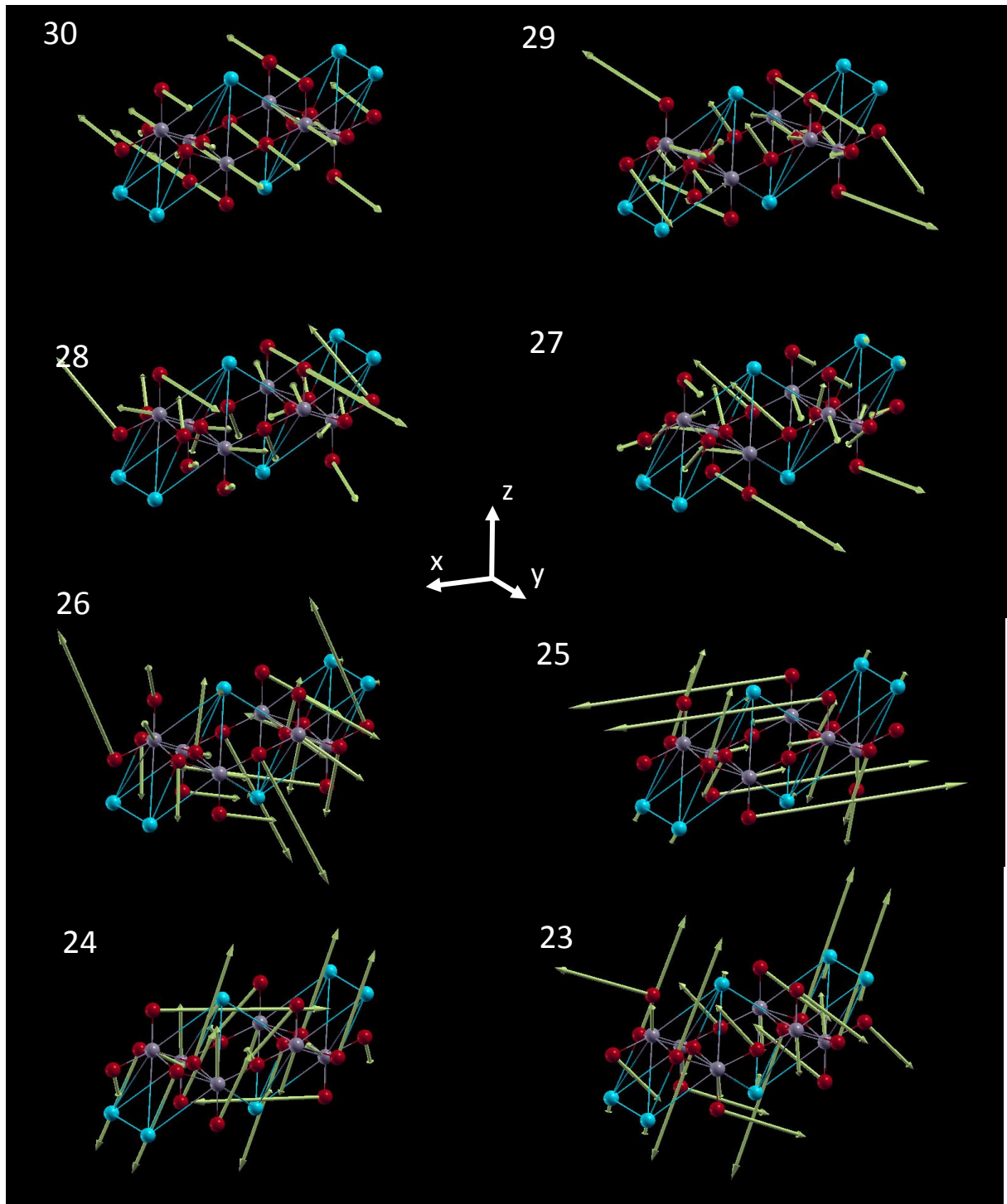


Figure 18. Representations of the vibrational phonon modes N° 30, 29, 28, 27, 26, 25, 24 and 23 calculated using Density Function Theory for $\text{Rb}_2\text{Ti}_2\text{O}_5$ system. The frequency and Raman intensity of the related phonon modes are displayed in the table [XII](#)

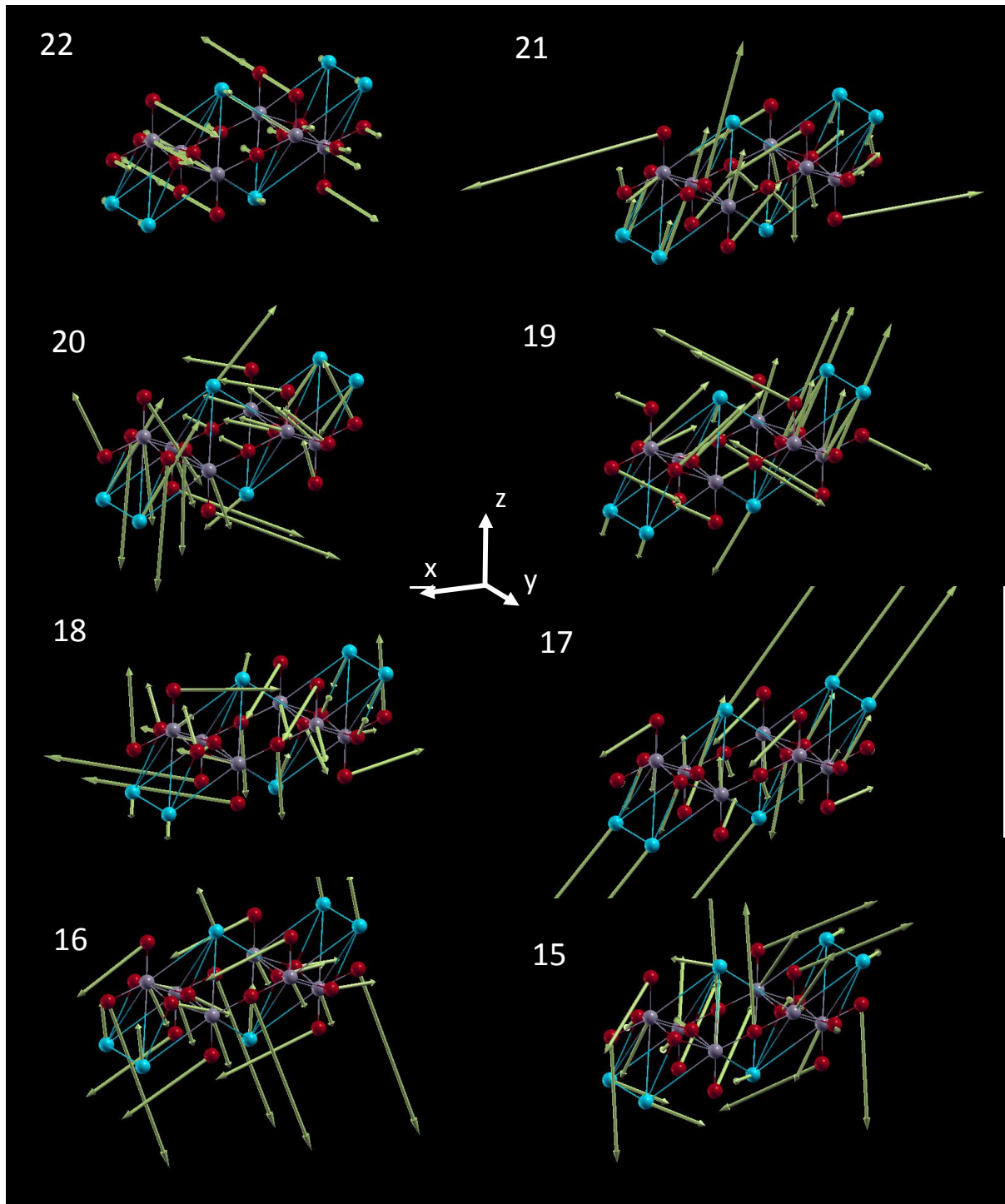


Figure 19. Representations of the vibrational phonon modes N° 22, 21, 20, 19, 18, 17, 16 and 15 calculated using Density Function Theory for $\text{Rb}_2\text{Ti}_2\text{O}_5$ system. The frequency and Raman intensity of the related phonon modes are displayed in the table [XII](#)

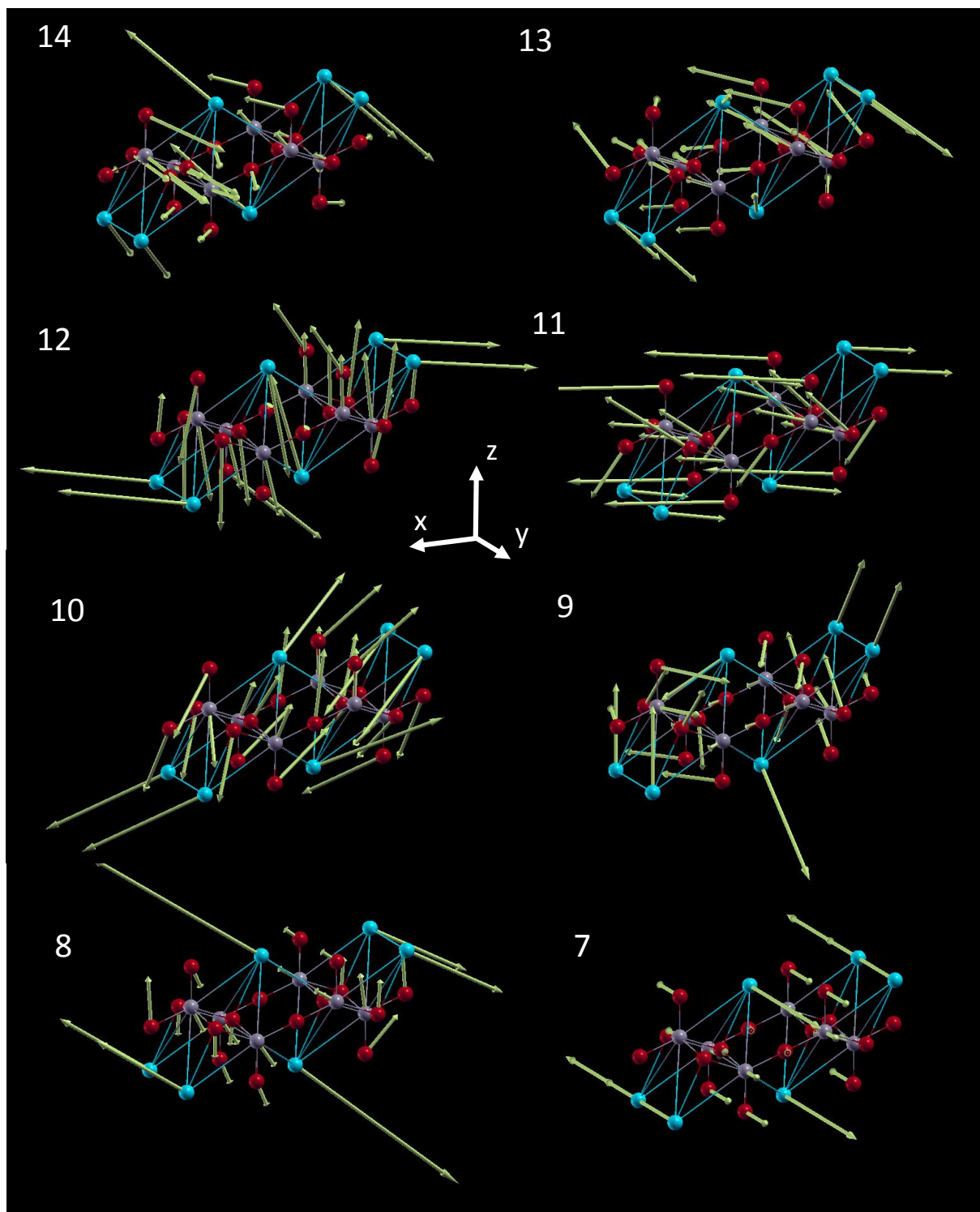


Figure 20. Representations of the vibrational phonon modes N° 14, 13, 12, 11, 10, 9, 8 and 7 calculated using Density Function Theory for $\text{Rb}_2\text{Ti}_2\text{O}_5$ system. The frequency and Raman intensity of the related phonon modes are displayed in the table [XII](#)

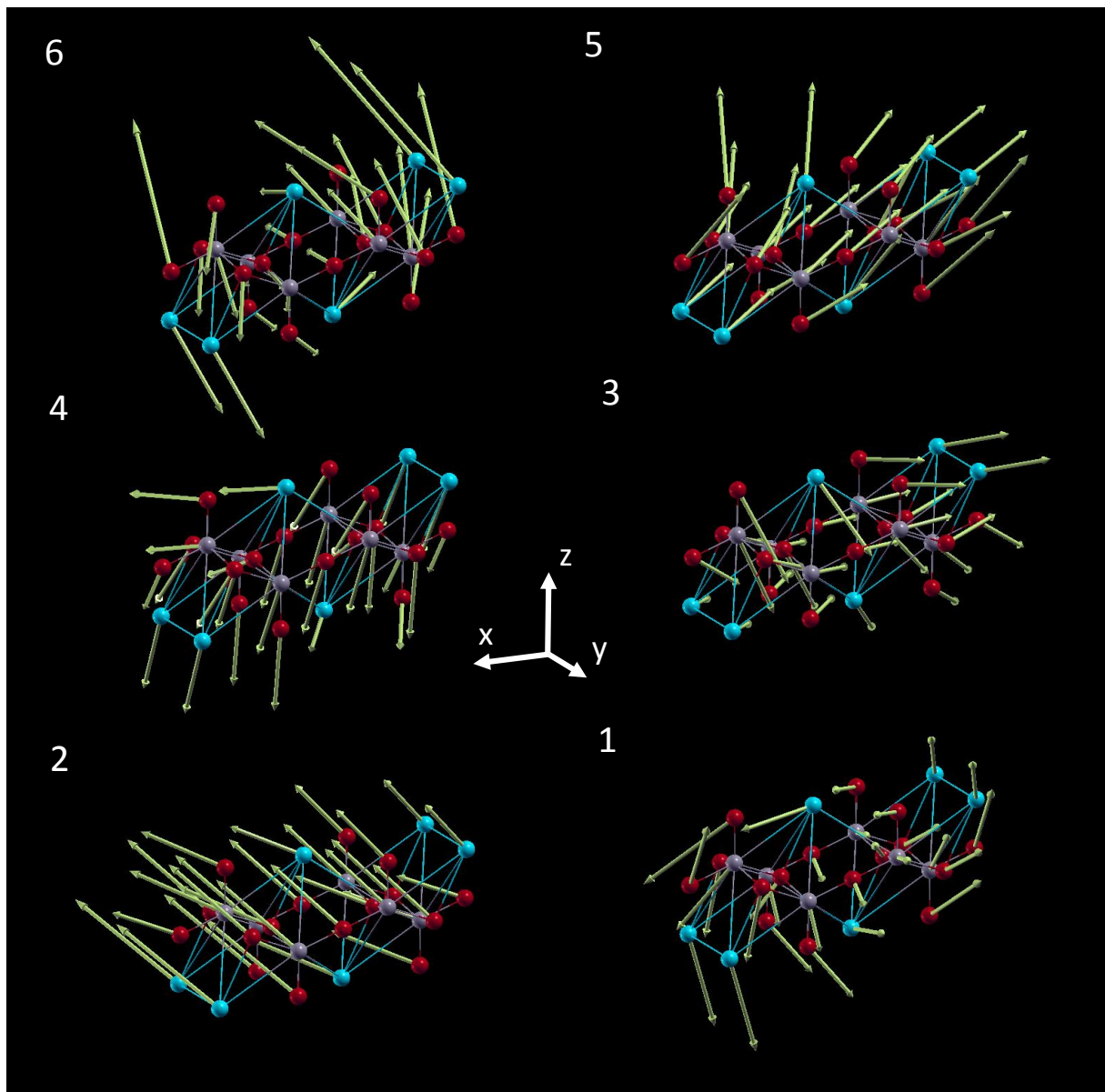


Figure 21. Representations of the vibrational phonon modes N° 6, 5, 4, 3, 2 and 1 calculated using Density Function Theory for $\text{Rb}_2\text{Ti}_2\text{O}_5$ system. The frequency and Raman intensity of the related phonon modes are displayed in the table [XII](#)